Current Chemistry Letters 12 (2023) 235–248

Contents lists available atGrowingScience

Current Chemistry Letters

homepage: www.GrowingScience.com

Gallic acid-butyramide monohydrate cocrystal: Crystal growth, Structural insights, Theoretical calculations and Molecular docking studies against COVID-19 main protease

K.L. Jyothi[a,b], M.K. Hema[a], Karthik Kumara[c] and N.K. Lokanath[a*]

[a]*Department of Studies in Physics, University of Mysore, Manasagangotri, Mysuru - 570 006, India*
[b]*Department of PG Physics, Government First Grade College and PG Center, Chintamani - 563125, India*
[c]*Department of Physics, B.M.S. College of Engineering, Bengaluru – 560019, India*

C H R O N I C L E

Article history:
Received February 30, 2022
Received in revised form
April 18, 2022
Accepted June 20, 2022
Available online
June 20, 2022

Keywords:
Cocrystals
Hydrogen bonding interactions
3D Energy framework
DFT studies
COVID-19 main protease

A B S T R A C T

Single crystal X-ray diffraction is the only experimental technique available to elucidate the complete three-dimensional structure of the samples at molecular and atomic levels. But this technique demands defect-free single crystals. Growing good quality single crystals which are suitable to collect X-ray intensity data is an art rather than science. Among the various crystal growth methods, the most effective and commonly used is the slow evaporation method. Using this method, defect-free single crystals of the ground mixture of gallic acid (GA) and butyramide (BU) taken in a 1:1 molar ratio are obtained. The compound was subjected to experimental characterizations like; PXRD, FTIR, SCXRD, and TGA. Further, these results were utilized in the computational characterizations namely, Hirshfeld surface analysis, interaction energy calculations, DFT studies, and docking studies. Structural characterization revealed that the GA-BU compound was crystallized as a cocrystal hydrate with 2:1:1 stoichiometry in a monoclinic crystal system and P21/n space group. Structural studies exposed the presence of various inter and intramolecular hydrogen bond interactions, ring synthons, DDAA environment of the water molecule, and π ... π stacking interactions. The contribution of the several close contacts to the crystal structure, the influence of different interaction energies in the packing, the HOMO-LUMO energy gap, and the location of reactive sites were realized through computational studies. Further, a molecular docking study has been performed to check the antiviral activity of the title compound against COVID-19.

1. Introduction

Growing single crystals is an art rather than a science, which begins with the nucleation process in which atoms/ions/molecules of the solute dissolved in the suitable solvent start to assemble into a cluster on a microscopic scale[1,2]. The region where the initiation of nucleation takes place is called the nucleation site and as time elapses, the size of the crystal increases. This subsequent increase in the size of the nuclei is known as crystal growth. Both nucleation and crystal growth depend on the supersaturation state of the solution[3,4]. The solubility of the solute in a solvent depends on the saturation level of the solution, which depends on temperature, concentration, ionic strength of the solute, and polarity of the solvent. The most common crystal growth methods used to obtain good quality single crystals are slow evaporation, slow cooling, solvent diffusion, vapor diffusion, sublimation, and convection[5]. These crystal growth techniques play a very important role in the structure determination of the novel compounds and help in establishing the structure-function correlation. In nature, we come across many compounds with medicinal values which can't be directly used as drugs[6]. This is because of the poor performance parameters such as solubility, dissolution, and bioavailability. These compounds are known as active pharmaceutical ingredients (APIs)[7]. The performance of these APIs as drugs can be enhanced by altering their physicochemical properties without disturbing their inherent medicinal values. This can be achieved by preparing

* Corresponding author.
E-mail address lokanath@physics.uni-mysore.ac.in (N.K. Lokanath)

doi: 10.5267/j.ccl.2022.6.004

multicomponent compounds of the APIs using suitable bio-acceptable organic compounds as coformers[8,9]. When API and coformers are connected through non-covalent intermolecular interactions (such as hydrogen bonding, pi. . .pi, and van der Wall interactions), resulting in the formation of a supermolecule, we obtain multicomponent compound[10,11]. Further, two major regulatory agencies, the United States Food and Drug Administration (US FDA) and European Medical Agency (EMA) have advocated and approved the drug status for many multicomponent forms of API as drug intermediate[12].
From the literature survey and Cambridge Structural Database (CSD) analysis, we found an interesting API, a phenolic acid with one carboxylic acid and three phenol functional groups known as gallic acid (GA). This compound exhibits important biological activities like antioxidant, anti-inflammatory, antiviral, antibacterial, anticancer, and antidiabetic[13-18]. Further, gallic acid found applications in the treatment of allergic diseases like asthma and allergic rhinitis[19]. With four hydrogen bonding donor and acceptor sites, gallic acid is identified as the most suitable compound to use as one of the components in the preparation of multicomponent compounds. Further, it was observed that most of the drugs on the market contain amides because of their reduced allergenic characteristics and greater potency at lower concentrations. Also, as amide compounds can easily involve in the formation of various supramolecular synthons with carboxylic acid compounds, we selected butyramide (BU) as a coformer in our work[20,21]. Expected supramolecular synthons between these pure compounds through intermolecular hydrogen bonding interactions were illustrated in **Fig. 1**.

In the present research work, a binary compound of gallic acid and butyramide was prepared using mechanochemical grinding and single crystals were obtained by a slow evaporation method. Novel compound preparation has been characterized through PXRD and FTIR methods. The grown crystals of the title compound were then characterized using SCXRD and TGA techniques and finally experimental results were used to carry out theoretical analysis such as; DFT, Hirshfeld surface analysis followed by docking studies.

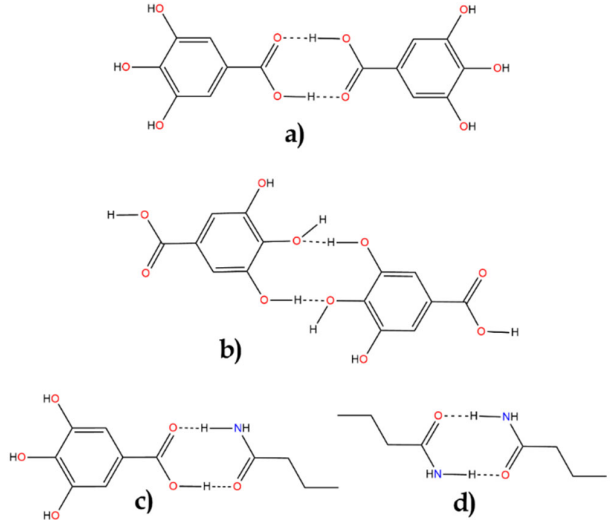

Fig. 1. Excepted supramolecular ring synthons between GA molecules (a and b), GA and BU molecules (c) and BU molecules (d)

2. Results and Discussion

2.1 Powder X-ray diffraction

The diffracted X-ray intensity peaks at 2θ positions (**Fig. S1**) of the pure compounds and that of the binary compound prepared were analyzed and compared. The PXRD pattern of gallic acid (GA) showed peaks at 2θ positions 8.130º, 11.995º, 16.211º, 19.123º, 19.775º, 25.497º, 27.756º, 28.057º. Whereas, the PXRD pattern of butyramide (BU) showed diffraction peaks at 2θ positions 8.931º, 17.721º, and 23.598º. Distinct peaks in the PXRD pattern of the binary compound at 2θ positions 6.478º, 10.004º, 19.050º, 20.123º, 23.087º, 24.825º, 26.205º, 27.227º confirmed its new crystal phase. Further, the PXRD pattern from the crystal structure was simulated using the mercury software and is compared with the experimental one. The experimental and theoretical PXRD patterns were found identical and this certified the purity of the compound.

2.2 Fourier transform infrared spectroscopy

The FTIR spectrum of gallic acid, butyramide coformer, and their mixture between 400-4000 cm^{-1} range are shown in **Fig. S2.** The characteristic absorption peaks for the functional groups were assigned and are listed in **Table 1**. The shift in the absorption bands of all the functional groups and the presence of several other bands were noticed. These observations

supported the formation of a novel compound and the existence of hydrogen bond interactions between gallic acid and butyramide.

Table 1. FTIR major band assignment of starting and multicomponent compounds (cm^{-1})

Sample	ν_{O-H} (Alcohol)	ν_{O-H} (Acid)	$\nu_{C=O}$ (Acid)	ν_{C-O} (Acid)	ν_{N-H} (Bending)	ν_{N-H} (Stretching)	$\nu_{C=O}$ (Amide)
GA	3345.27	3273.45	1700.25	1239.40	-	-	-
BU	-	-	-	-	1637.94	3367.35	1667.24
GA-BU	3485.83	3368.08	1697.05	1269.26	1613.94	3371.76	1643.95

2.3 Single-crystal X-ray diffraction studies

A good quality needle-shaped single crystal of dimensions 0.25 × 0.20 × 0.31 mm of GA-BU compound, prepared by taking the pure components in a 1:1 molar ratio, was selected using a polarised microscope for X-ray diffraction studies, and the complete intensity data were collected and the crystal structure was solved. The GA-BU compound was found to be crystallized in a monoclinic system with a $P2_1/n$ space group. Overall 292 parameters were refined with 3232 unique reflections converged to residual in solving crystal structure. The GA-BU compound was crystallized as a cocrystal monohydrate with four (2GA, 1BU, and $1H_2O$) molecules with an empirical formula $2(C_7H_5O_5)\cdot C_4H_9NO\cdot H_2O$ in the asymmetric unit with 2:1:1 stoichiometry. The unit cell parameters of the cocrystal hydrate are $a = 7.6802(3)$ Å, $b = 27.1860(4)$ Å, $c = 9.7855(4)$ Å and $\beta = 108.849(7)^o$. Structural information of the GA-BU cocrystal hydrate is mentioned in **Table S1.** The ORTEP (Oak Ridge Thermal Ellipsoid Plot) of the cocrystal hydrate molecule with hydrogen bonding interactions involved in the asymmetric unit is shown in **Fig. 2**. Two strong O5-H5…O6 (d/Å, θ /°; 2.625, 154) and O7-H7…O4 (d/Å, θ /°; 2.619, 151) hydrogen bond interactions between the two gallic acid molecules formed a $R_2^2(8)$ motif. Further, this ring motif is connected to the BU molecule through O1-H1…O12 (d/Å, θ /°; 2.683, 166) and then the BU molecule is connected to the water molecule through O11-H11A…O12 (d/Å, θ /°; 2.691, 170) intermolecular hydrogen bonds.

The parameters of various inter and intramolecular hydrogen bond interactions that contributed to the formation of GA-BU cocrystal hydrate are listed in **Table 2**. The packing of molecules in the crystal structure as viewed along the crystallographic *a*, *b,* and *c* axes are shown in **Fig. S3**. Acid-dimers are further connected through a supramolecular ring synthon with graph set notation R_1^1 (6) and formed a staircase network resulting in the formation of a hexagonal-shaped void supramolecular assembly down the crystallographic *a*-axis and is as shown in **Fig. 3.** Structural analysis revealed the involvement of the water molecule in four hydrogen bond interactions; N1- H1C…O11 (d/Å, θ /°; 2.855, 123), O10-H10…O11 (d/Å, θ /°; 2.724, 163), O11-H11A…O12 (d/Å, θ /°; 2.691,170) and O11-H11B…O10 (d/Å, θ /°; 2.724, 159) as a donor in two interactions and as an acceptor in the remaining two interactions respectively. Thus the role of the water molecule with its DDAA environment (**Fig. 4)** has proved its contribution to the formation of this molecule. Further, the hydrogen bonding interaction of water molecules with GA and BU molecules resulted in the formation of a three-dimensional packing network of the molecules. The detailed structural studies have shown the presence of two $\pi\ldots\pi$ stacking interactions between the centroid of two gallic acid molecules. The centroid, Cg1 (of the atoms C1, C2, C3, C4, C5, and C6) of the one gallic acid molecule has been involved in two $\pi\ldots\pi$ stacking interactions with the centroid, Cg2 (of the atoms C9, C10, C11, C12, C13, and C14) of the second gallic acid molecule. The parameters of these two interactions are; Cg1… Cg2 = 3.871 Å; symmetry code:1-x, 1-y, 1-z and Cg1…Cg2 = 3.811 Å; symmetry code : 2-x, 1-y, 1-z and are shown in the **Fig. 5.** Further, bond lengths, bond angles, and torsion angles of the non-hydrogen atoms are listed in **Tables S2, S3** and **S4** respectively.

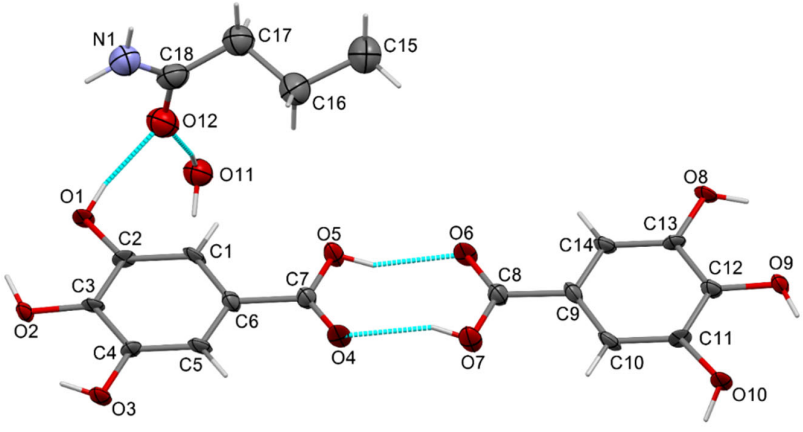

Fig. 2: ORTEP of GA-BU cocrystal hydrate drawn at 50% probability with intermolecular hydrogen bonding interactions (blue colored dotted lines)

2.4 Thermogravimetric analysis

Thermogram of gallic acid - butyramide cocrystal was obtained and its thermal properties were analyzed. A three-step thermogram of GA-BU cocrystal hydrate which represents the weight loss versus temperature is shown in **Fig. S4**. Weight loss of 5% in the temperature range of 72-100ºC corresponds to a loss of one molecule of water, as the theoretical mass loss for the dehydration of one molecule of water from the crystal lattice of GA-BU is 4.06%[22]. The loss of crystalline water leads to the dissociation of cocrystal. In the second step weight loss of 67% was observed in the temperature range of 185-318ºC. This can be attributed to the degradation/sublimation of two moles of gallic acid (theoretical weight loss is 76.75%). Further, the third and final step weight loss of 13% was observed in the temperature range of 319-420ºC and this indicates the degradation/sublimation of one mole of butyramide (theoretical weight loss is 17.81%). Finally, a total weight loss of 90% was observed from the thermogram. Further, the presence of one molecule of water in the crystal lattice of GA-BU cocrystal hydrate has been confirmed from the single crystal X-ray diffraction analysis.

Table 2. Hydrogen bond geometry of GA-BU cocrystal hydrate.

Atoms	D – H (Å)	H…A (Å)	D-H…A (Å)	D-H…A (°)	Symmetry
O1-H1…O12	0.82	1.88	2.683(6)	166	-
N1-H1B…O9	0.86	2.37	3.140(9)	149	3/2- *x*, 1/2+ *y* 3/2- *z*
N1-H1C…O11	0.86	2.29	2.855(9)	123	-1+*x*, *y*, *z*
O2-H2…O1*	0.82	2.38	2.748(7)	108	-
O2-H2…O8	0.82	1.99	2.766(7)	158	3/2-*x*, 1/2+*y*, 3/2-*z*
O3-H3…O2*	0.82	2.33	2.713(6)	109	-
O3-H3…O1	0.82	1.96	2.713(6)	152	-1/2+*x*, 3/2-*y*, -1/2+*z*
O5-H5…O6	0.82	1.86	2.625(6)	154	-
O7-H7…O4	0.82	1.87	2.619(7)	151	-
O8-H8. . .O9*	0.82	2.28	2.721(6)	114	-
O8-H8…O10	0.82	1.97	2.733(7)	154	1/2+*x*, 1/2-*y*, 1/2+*z*
O9-H9…O10*	0.82	2.26	2.698(6)	114	-
O9-H9…O3	0.82	2.08	2.753(7)	140	3/2-*x*, -1/2+*y*, 1/2-*z*
O10-H10…O11	0.82	1.93	2.724(7)	163	2-*x*, 1-*y*, 1-*z*
O11-H11A…O12	0.85	1.85	2.691(8)	170	-
O11-H11B…O10	0.85	1.91	2.724(7)	159	2-*x*, 1-*y*, 1-*z*
C1-H1A…O12	0.93	2.59	3.232(8)	127	-
C1-H1A…O5*	0.93	2.47	2.779(7)	100	-
C14-H14…O6*	0.93	2.48	2.787(7)	100	-

* Intramolecular interaction.

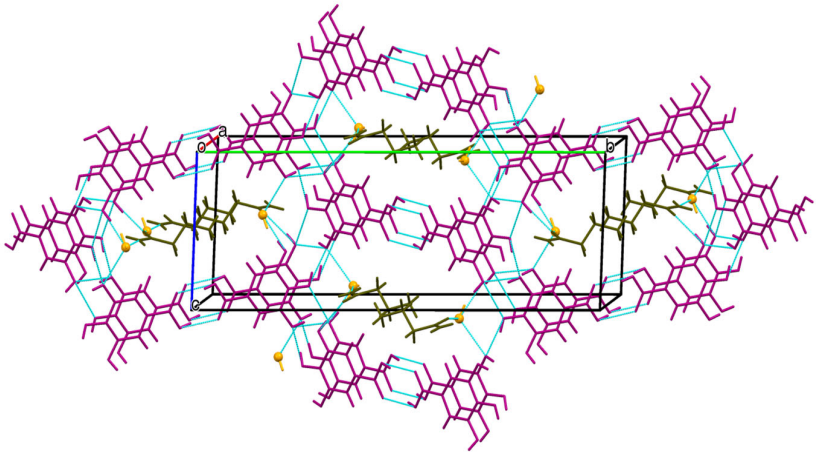

Fig. 3. Three dimentional packing of the molecules through variuos supramolecular ring synthons, when viewed down the crystallographic a-axis

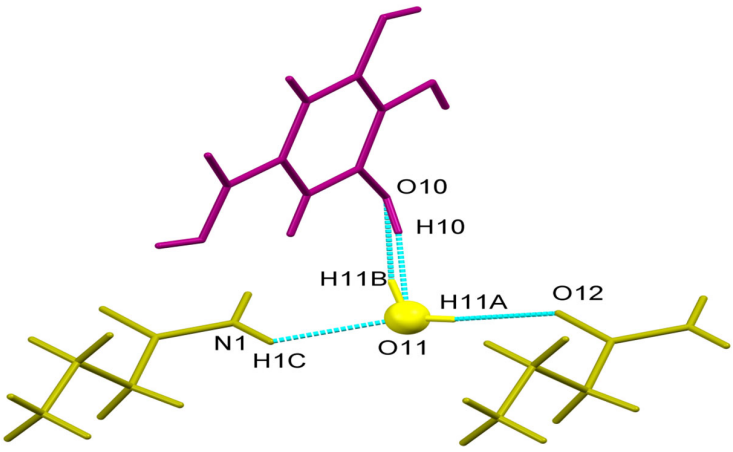

Fig. 4. DDAA environment water molecule in the crystal structure

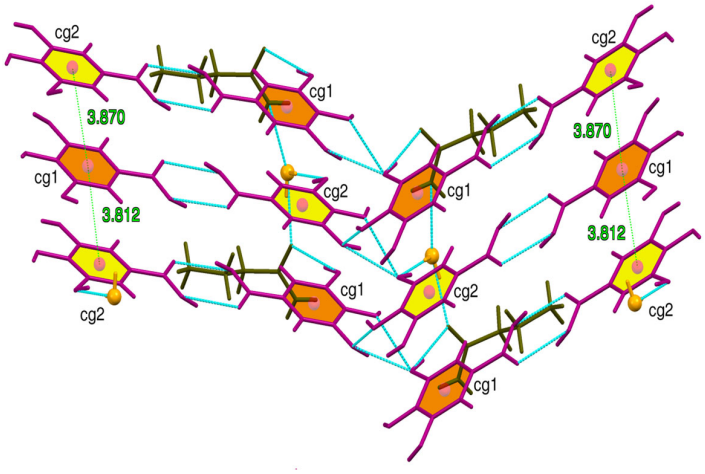

Fig. 5. $\pi\ldots\pi$ stacking interactions between GA molecules in the GA-BU cocrystal hydrate

2.5 Hirshfeld surface analysis

Hirshfeld surface analysis (HSA) is one of the best methods for the investigation of intermolecular interactions in the crystalline environment. The presence of water molecules and coformer in the cocrystal moiety requires HSA, to understand the nature and individual contributions of each intermolecular interaction. Insights from HSA are even more necessary to understand the structural stability of the molecule through O-H…π, C-H…π, and $\pi\ldots\pi$ stacking interactions.

Computation and analysis of the Hirshfeld surface were carried out by loading the crystallographic information input file to the *CrystalExplorer* 17.5 software[23]. The d_{norm} plots were mapped with colour scale between −1.2073 au (blue) to 1.1879 au (red) respectively. The expanded 2D fingerprint plots (FPs)[24,25] was drawn in the range of 0.6 - 2.8 Å view with the d_e and d_i distance scales displayed on the graph axes. The calculated volume inside the Hirshfeld surface is found to be 475.26 Å^3 in the area of 441.41 Å^2.

The analysis of 2D fingerprint plots revealed the quantitative contributions of molecular contacts to the total Hirshfeld surface. The H…H (38.0%) contacts have maximum and N…O (0.2%) have minimum contributions. Similarly, the O…H (35.8%), C…C (8.7%), C…H (8.1%), O…O (4.2%), C…O (3.7%), and N…H (1.1%) contacts also contribute to the total Hirshfeld surface as shown in **Fig. 6.** These inter contacts are highlighted on the molecular Hirshfeld surface using conventional mapping of d_{norm} (-1.2073 au to +1.1879 au), shape index (-1.0 au to +1.0 au), curvedness (-4.0 au to +0.4 au), d_i (0.4319 au to 2.3733 au), d_e (0.4322 to 2.3731 au) and fragment patches (0.1 au to 30 au) as shown in **Fig. 7.** The coloured regions on the molecular surfaces can be identified to analyze the specific characteristic interactions of the molecular surface. The regions with red and blue color on the d_{norm} correspond to the shorter and longer inter contacts, the white color indicates the contacts around the van der Waals radii. Similarly, the shape index mapped on the Hirshfeld surface indicates the red triangle concave regions of stacking interactions and the blue triangle convex regions of the ring atoms of the molecule. The root mean square value of the curvature for the surface is the curvedness (low with a flat area and high with sharp curvature) which divides the surface into contact patches with the nearest molecule. The flat regions of the surface

indicate the π…π stacking interactions[26-28]. The fragment patches on the molecule correspond to the different molecular interactions over the molecular surface.

The O-H…*π,* C-H…*π,* and *π*…*π* stacking interactions[24] are evidently shown in FPs. The inter-contact distances calculated from HSA are in good agreement with the values obtained from the experimental X-ray structure studies (Table 3). The two spikes with points at d_e and d_i in the FPs illustrate that the value of $d_e + d_i$ to be 2.8 Å (1.7 + 1.1) for C…H interactions, 1.8 Å (1.1 + 0.7) for O…H interactions and 3 Å (1.7 + 1.3) for N…H interactions in the donor and acceptor regions of the FPs. These molecular interactions serve as a bridge between gallic acid, butyramide, and water molecules in the crystalline environment leading to the formation of supramolecular synthons. The intermolecular interactions are highlighted on the molecular Hirshfeld surface using conventional mapping of d_{norm} as shown in **Fig. S5.**

2.6 Interaction energies and 3D energy frameworks

The interaction energy of the molecules can be obtained with the help of the known procedure[29-31] using the *CrystalExplorer* 17.5 software. The total interaction energy was calculated by generating the molecular cluster of radii 3.8 Å around the selected molecule (**Fig. S6**). The symmetry operations were employed in the energy framework calculations to compute the molecular wave functions and to generate electron densities of the cluster of molecules present around the selected molecule using the CE-B3LYP/6-31G(d,p) energy model with the scale factors to determine E_{tot} : k_{ele} = 1.057, k_{pol} = 0.740, k_{dis} = 0.871, k_{rep} = 0.618[32].

The total interaction energy is found to be -277.902 kJ mol^{-1} with the electrostatic (-385.065 kJ mol^{-1}), polarization (-49.432 kJ mol^{-1}), dispersion (-162.354 kJ mol^{-1}), and repulsive (318.95 kJ mol^{-1}) energy calculated by energy frameworks analysis. The energy frameworks of the molecule were produced for electrostatic, dispersion and total energies and represented in terms of different colored cylinders with a scale factor (cylinder tube size) of 100 and cut-off energy -150 kJ/mol. These cylinders correspond to the magnitude of the interaction energy between molecular pairs and the strength of the molecular packing along with different directions of the molecular arrangements. The molecular cluster with red cylinders represents the electrostatic energy (E_{elec}), green color cylinders represent dispersive energy (E_{dis}) and blue cylinders represent the total interaction energy of the molecule (**Fig. 8**). The energy framework calculations revealed that the electrostatic energy dominates over the dispersion and polarization energies in the crystalline environment[32].

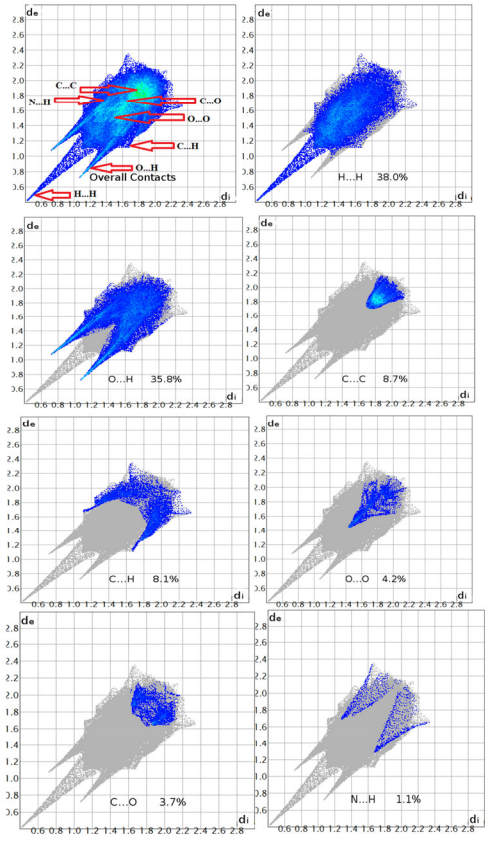

Fig. 6. 2D Fingerprint plots of the title compound showing the individual contribution of each interaction to the total Hirshfeld surface

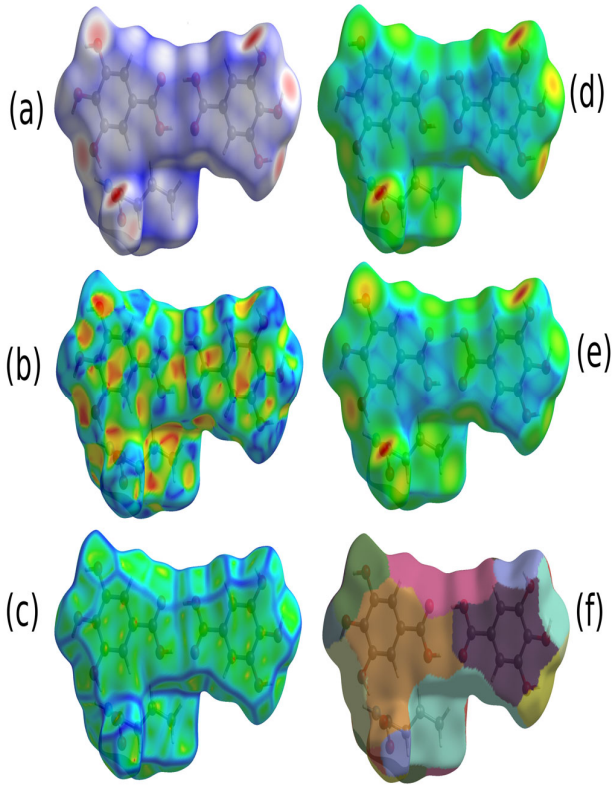

Fig. 7. d_{norm} (a), Shapeindex (b), curvedness (c), d_i surface (d), d_e surface (f), fragment patches (e) mapped on Hirshfeld surface of the molecule

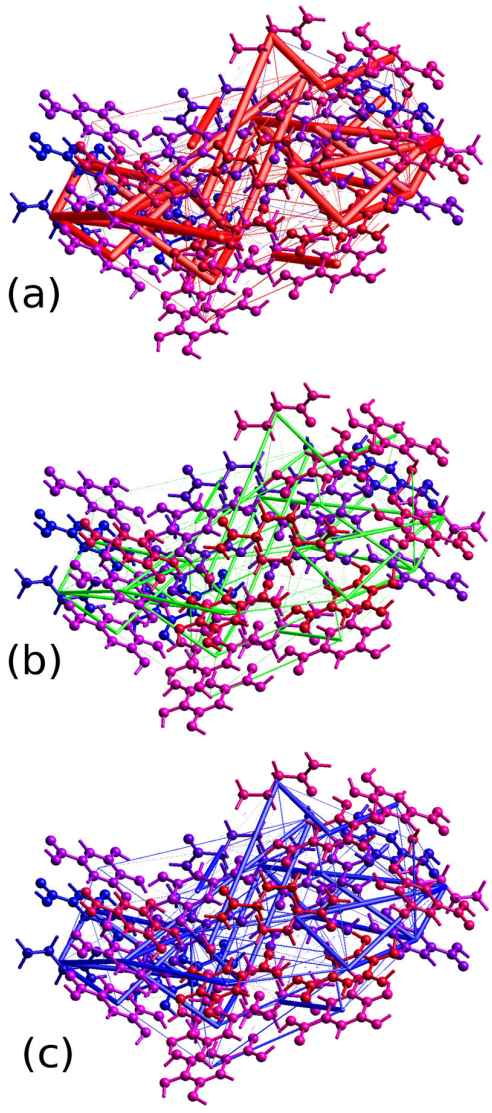

Fig. 8. The energy frameworks for electrostatic energy (a), dispersion energy (b) and total energy (c) of the molecule

2.7 Density functional theory calculations

To obtain more awareness about the electronic structure of the GA-BU cocrystal hydrate, density functional theory calculations were performed. The results of the geometry optimization were analyzed and compared with that of the experimental. The optimized structure is found identical to the experimental structure (**Fig. 9a**) and the experimental geometrical parameters namely, bond lengths, bond angles, and torsion angles of the cocrystal hydrate are well correlated with the optimized structure with correlation coefficients of 0.9689, 0.9179, and 0.9997 (**Tables S2, S3, and S4**) respectively. The theoretical C-N bond length in the BU molecule, C9-C14, and C6-C5 bond lengths in the GA molecules deviated by 0.039Å, 0.041Å, and 0.045Å from the XRD results. The small deviation in the bond angles (XRD/DFT) around the carbon atoms (C7 and C9) of the carboxylic acid group of both the GA molecules (O4-C7-C6 = 119.9/122.5°, O5-C7-C6 = 116.6/114.6°, O6-C8-C9 = 120.3/122.4° and O7-C8-C9 = 116.1/114.3°) shows the interaction between the GA molecules. Further, a small deviation in the bond angle around the carbon atom of the C=ONH$_2$ (amide) group of the BU molecule (N1-C18-C17 = 120.1/117.5° and O12-C18-N1 = 119.0/121.0°) has shown its interaction with the neighboring GA and water molecules. For GA molecules in the GA-BU cocrystal hydrate, all the torsion angles are almost equal to 180° or 0° which shows the planar structure of the GA molecules, whereas the BU molecule is found to be non-planar. The

calculated scaled wavenumbers of vibrational IR bands of the molecules are assigned from the frequency optimization and are compared with the experimental results.

The frontier Kohn-Sham molecular orbital structures are obtained for both starting compounds and the novel cocrystal hydrate. The HOMO-LUMO energy gap of 4.8629 eV and 6.8758 eV is observed for GA and BU molecules whereas, for GA-BU cocrystal hydrate 4.6749 eV is observed (**Fig. 9b**). This result indicates that the cocrystal hydrate molecule is chemically more reactive and kinetically less stable when compared with that of the starting compounds. Quantum chemical reactive parameters of both starting molecules and the novel cocrystal hydrate are described in **Table 3**. Furthermore, to identify the electrophilic and nucleophilic active sites, a molecular electrostatic potential (MEP) map (**Fig. 9c**) was also generated on the basis of the electron density of the GA-BU cocrystal hydrate molecule. The color region red<orange<yellow<green<blue in the 3D MEP map is a measure of the electrostatic potential value in increasing order. The electrophilic (negative) active regions are mainly observed as reddish yellow colored region around the oxygen atom whereas, the nucleophilic (positive) active regions are observed as dark and light blue colored region around $–NH_2$ functional group and the hydrogen atoms as shown in the figure[33].

Table 3. HOMO/LUMO energy and related molecular properties of GA, BU and GA–BU cocrystal hydrate

Parameter	GA	BU	GA–BU
E_{HOMO} (eV)	–6.7101	–7.1155	–6.2551
E_{LUMO} (eV)	–1.8471	–0.2397	–1.5802
Energy gap (Δ) (eV)	4.8629	6.8758	4.6749
Ionization energy (I) (eV)	6.7101	7.1155	6.2551
Electron affinity (A) (eV)	1.8471	0.2397	1.5802
Electronegativity (χ) (eV)	4.2786	3.6776	3.9176
Chemical potential (μ) (eV)	–4.2786	–3.6776	–3.9176
Global hardness (η) (eV)	2.4315	3.4379	2.3375
Global softness (s) (eV^{-1})	0.4113	0.2909	0.4278
Electrophilicity index (ω) (eV)	3.7644	1.9670	3.2830

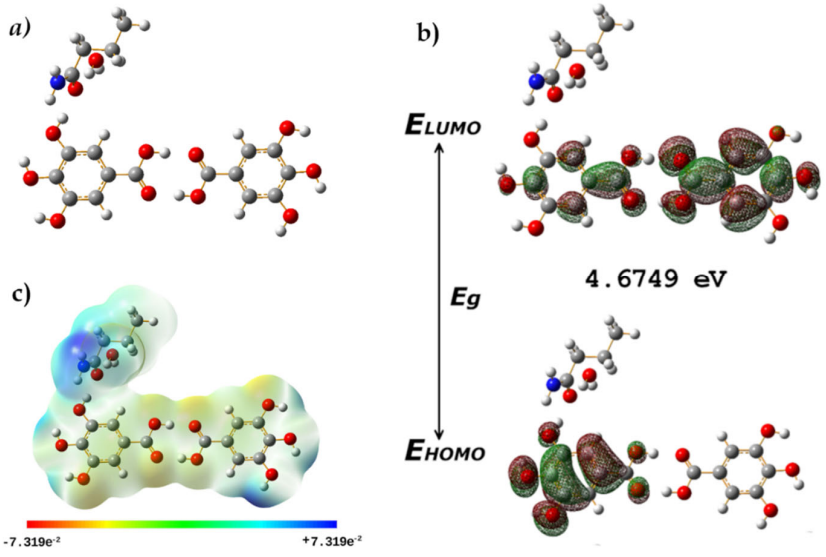

Fig. 9. a) Optimized structure, b) HOMO-LUMO energy gap and c) Molecular potential map of GA-BU cocrystal hydrate

2.8 Molecular docking studies

The characteristics of the best docking pose for the cocrystal and its binding pocket is analyzed by comparing with the binding mode of N3 inhibitor in the active site of 6LU7. N3 inhibitor in the main protease interacts with the catalytic dyad (CYS-145 and HIS-41) of the main protease through hydrophobic and hydrogen bond interactions. Molecular docking analysis reveals that the π system of the benzene ring in GA-BU cocrystal interacts with the CYS-145 residue of the main protease (4.85 Å). GA-BU cocrystal strongly binds to the active pocket of the main protease (**Fig. 10**) with the conventional hydrogen bonds having the binding energy of -9.5 kcal/mol between the GA-BU-6LU7 complex. The significant interactions between GA-BU cocrystal and the main protease are described by five hydrogen bond interactions between HIS166, LEU14, GLY143, GLN189, and HIS163 residues and the OH groups of GA-BU (**Table 4**). Main protease and cocrystal binding are also stabilized by π-alkyl interaction between PRO168 residue of 6LU7 and benzene π of GA-BU (table and figure).

Table 4. Glide docking interaction details between main protease and selected GA-BU

Protein (Amino Acid)	Ligand	Interaction Type	Distance (Å)	Binding score (kcal/ mol)
HIS166	OH (O9)	Conventional	2.19	
LEU141	OH (O5)	Conventional	2.62	
LEU141	OH (O1)	Acceptor-acceptor	2.71	
GLY143	OH (O3)	Conventional	2.75	
GLN189	OH (O19)	Conventional	2.75	-8.1
HIS166	OH (O5)	Conventional	2.19	
CYS145	Centroid of the ring	π-Alkyl	4.85	
PRO168	Centroid of the ring	π-Alkyl	5.10	

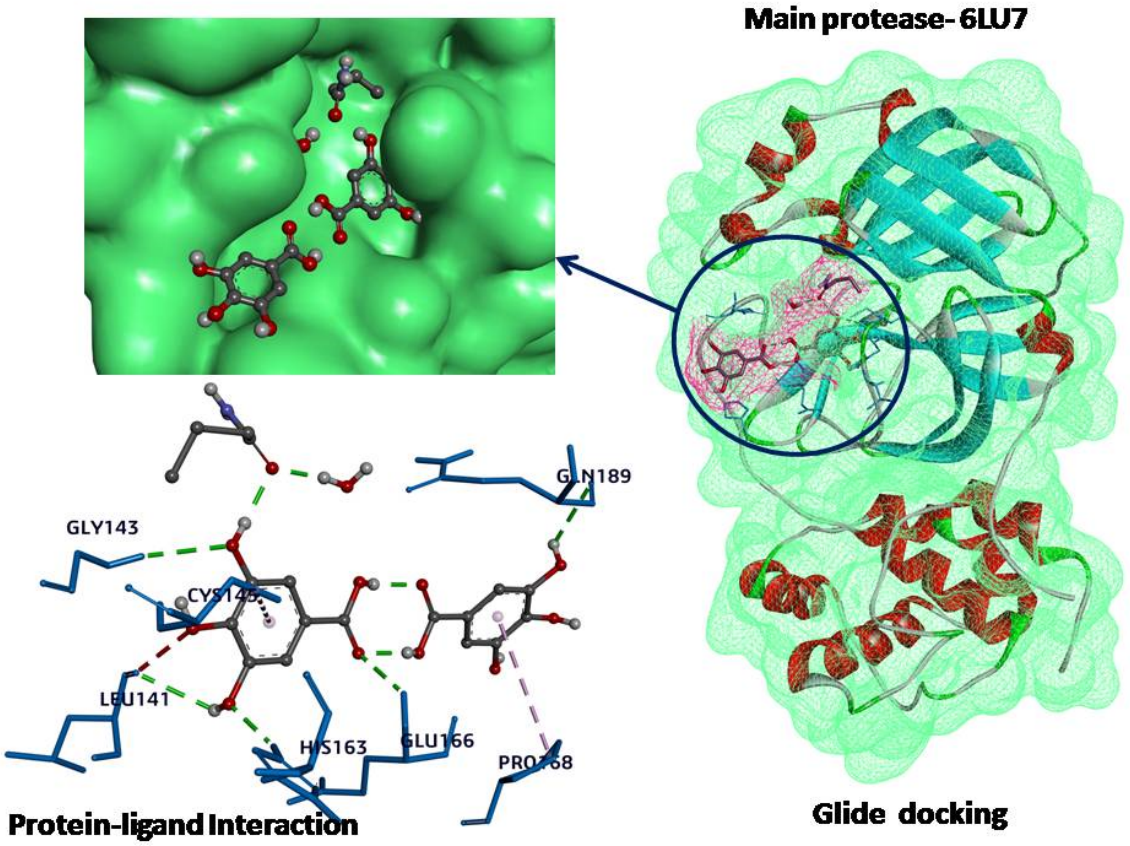

Fig. 10. Glide docking and interaction model between GA-BU and main protease of covid-19

3. Conclusion

In the present study, we have prepared a binary compound of gallic acid and butyramide mechanochemical grinding methods. The formation of the novel compound was supported by PXRD, FTIR techniques, and confirmed by the single-crystal X-ray diffraction method. Crystal structure studies revealed that the title compound was crystallized as a cocrystal hydrate in 2:1:1 stoichiometry in a monoclinic system with a $P2_1/n$ space group. Further, the interactions responsible for the stable crystal structure of the GA-BU cocrystal hydrate through the formation of the supramolecular synthons were explored from the analysis of crystal structure and molecular packing. The most stable hydrogen bonding synthon with graph set $R_2^2(8)$ was observed between the carboxylic acid groups. The Hirshfeld surface analysis revealed the contribution of each individual molecular interaction to the total generated molecular Hirshfeld surface. The major percentage contribution is found to be 38% from H…H interactions and the minor contribution is 0.2% from N…O interactions. Further, the interaction energies of the molecules were calculated within the radii of 3.8 Å and the 3D energy frameworks were analyzed. With the total interaction energy of -277.902 kJ mol^{-1} the electrostatic energy (-385.065 kJ mol^{-1}) dominates over the dispersion (-162.354 kJ mol^{-1}) and the polarization (-49.432 kJ mol^{-1}) energies in the crystalline environment. The HOMO-LUMO energy gap of the novel GA-BU molecule was found to be 4.6749 eV which revealed that the title compound possesses more kinetic and more reactive nature as compared with that of the gallic acid (API). A molecular docking study of the GA-BU molecule against the main protease of Covid-19 virus revealed the binding score of -9.5 Kcal/mol. The results suggest that GA-BU can proceed to further biological studies to test its potential against Covid-19 virus. Results of the present work offer a new avenue for the promising pharmaceutical applications of the GA-BU cocrystal hydrate which will be crucial for the development of better drugs.

Conflicts of interest

The authors declare no conflict of interest.

Acknowledgments

The authors would like to thank the National Diffractometer Facility, Department of Studies in Physics, UGC-MRP project (MRP-Phys2013-32718), University of Mysore, Mysuru, and Solid State and Structural Chemistry Unit, Indian Institute of Science, Bengaluru for providing infrastructure and instrumentation facilities.

4. Experimental section

4.1 Preparation and crystal growth

About 0.376 grams of gallic acid is taken with 0.17424 grams of butyramide to form a mixture of 1:1 molar ratio in a mortar. The mixture is subjected to manual neat grinding using a pestle for about 20min. Further, the mixture was subjected to liquid-assisted grinding for another 20min by adding a few drops of acetonitrile liquid[34-36]. Then the formation of the binary compound (GA-BU) in the new crystal phase in comparison with the pure initial compounds was confirmed from the PXRD technique and the novelty of the prepared compound was further confirmed from FTIR spectroscopic technique[37-38]. To obtain single crystals of the binary compound by slow evaporation method and to enhance the probability of nucleation during crystal growth methanol was chosen as the solvent on the basis of solubility considerations of the pure components of the binary compound. The supersaturated solution was prepared in a beaker and a magnetic stirrer was used to get a clear solution. Then the solution was kept undisturbed for slow and complete evaporation by covering the beaker with parafilm. Needle-shaped colorless single crystals of GA-BU having dimensions enough for the structural analysis were obtained in two weeks.

4.2 Powder X-ray diffraction (PXRD)

As every crystalline phase of a compound exhibits a unique powder X-ray pattern, the PXRD study is the most versatile and reliable technique to identify the formation of a novel crystalline phase[39]. PXRD patterns for the pure compounds (GA and BU) and acetonitrile ground binary compound (GA-BU) were recorded on a PAN analytical X'Pert diffractometer using Cu-Kα radiation (λ = 1.54056 Å), operated at 30 mA and 40 kV. Diffraction data were collected at room temperature over a 2θ range of 0-50° in continuous scan mode with a step size of 0.02°. Powder diffraction patterns were plotted and analyzed using X'Pert HighScore Plus.

4.3 Fourier transform infrared spectroscopy (FTIR)

Wavenumber values of the absorption peaks in the infrared spectrum, representing the functional groups are the IR signature of the compound. Therefore, the difference in the wavenumber values of the functional groups in the infrared spectrum between the initial compounds and the ground binary compound will prove the formation of the novel compound[40]. Hence, FTIR analysis was performed using PerkinElmer instrument, in the range of 4000 to 400 cm^{-1}. A resolution of 4 cm^{-1} was used to record the infrared spectra of the powder samples. Absorption peaks of the functional groups were identified, wavenumbers were assigned and tabulated for the analysis.

4.4 Single-crystal X-ray diffraction studies (SCXRD)

Good quality single crystal of the GA-BU compound was selected using a polarizing microscope. X-ray intensity data of the title compound were collected at 296 K on a Bruker Proteum2 CCD diffractometer with X-ray generator operating at 45 kV and 10 mA, using Cu-K_α radiation of wavelength 1.54178 Å. Data were collected for 24 frames per set with different settings of φ (0° and 90°), keeping the scan width of 0.5°, exposure time of 5 s, the sample to detector distance of 45.10 mm. The complete intensity data sets were processed using SAINT PLUS[41] and the absorption correction was conducted with the multi-scan method. The crystal structure was solved by the direct method, the position of all non-hydrogen atoms was identified and refined on F^2 by a full-matrix least-squares procedure using anisotropic displacement parameters by using SHELXS and SHELXL programs[42]. All the hydrogen atoms were located in difference Fourier maps and treated as riding on their atoms with isotropic thermal displacement parameters. The geometrical calculations were carried out using the crystallographic program PLATON[43]. The crystal packing diagrams were generated by the MERCURY software[44].

4.5 Thermogravimetric analysis (TGA)

Thermal stability is one of the important properties of the multicomponent crystals and it plays an important role in enhancing the performance parameters of the API[45]. Thermal properties like melting and decomposition points help in knowing the thermal stability of the crystals. These temperatures of the binary compound were identified using the thermogram of the GA-BU crystals, which is a graph of weight loss as a function of temperature. Further, from the same thermogram, one can investigate the presence of water and solvent molecules in the crystal. The value of final weight loss

will also help in deciding the purity of the components in the crystal. Therefore, thermogravimetric analysis was carried out by heating the crystals of GA-BU in the Mettler-Toledo TGA/SDTA 851e thermal analyzer under a flow of N_2 (40 ml min^{-1}). The crystals were heated at a rate of 10°C min^{-1} from 30°C to 600°C with inert alumina as a reference.

4.6 Hirshfeld surface studies, interaction energies, and 3D energy frameworks

Hirshfeld surface analysis (HSA) is an excellent tool to study the intermolecular interactions exhibited by the molecule in the crystalline environment. HSA serves as a key method for the calculation and the graphical visualization of the intermolecular interactions. The results obtained from HSA are very unique for each crystal structure. The HSA for the title cocrystal molecule was carried out by loading the crystallographic information file (CIF) to the *CrystalExplorer*[23] software. The electron distribution of the molecule was calculated using the sum of the spherical atom electron density to construct the molecular Hirshfeld surface. The molecular Hirshfeld surface mapped with 3D d_{norm} and 2D fingerprint plots (FPs) were produced based on d_e and d_i values, and the van der Waal's atomic radii (r) governed by the equation (1) given below, which enables to identify the regions of specific importance related to the intermolecular interactions. Here d_i is the distance from a given point on the Hirshfeld surface to the nearest nucleus inside the surface and d_e is the distance from a point to the nearest nucleus outside the surface. The colored spots on the d_{norm} surface represent different intermolecular interactions. The red region corresponds to the shorter contacts, the blue colored region represents the longer inter contacts whereas, the white region corresponds to the contacts around the van der Waal's radii. The fingerprint plot tells the contribution of each individual intermolecular interaction to the surface which can be recognized through color codes (frequency of presence) ranging from blue color (few points) through green color to red color (many points)[46-48]. HSA also helps to understand the stability of the crystal structure through O-H…π, C-H…π, and π…π stacking interactions. The d_i, d_e, shape index, curvedness surfaces and fragment patch of the Hirshfeld surface generated further shed light on the π-stacking interactions[49].

$$d_{norm} = \frac{d_i - r_i^{vdw}}{r_i^{vdw}} + \frac{d_e - r_e^{vdw}}{r_e^{vdw}} \quad (1)$$

Further, the molecular interaction energies in the crystalline environment were calculated from the monomer wave functions using CE-B3LYP/6-31G(d,p) for the 3D energy framework studies.

The molecular interaction energies such as electrostatic, polarization, dispersive, and repulsive energies were also computed which leads to the total interaction energy as given by

$$E_{tot} = E_{ele} + E_{pol} + E_{dis} + E_{rep}$$

$$E_{tot} = k_{ele}E'_{ele} + k_{pol}E'_{pol} + k_{dis}E'_{dis} + k_{rep}E'_{rep}$$

where, E'_{ele} represents the electrostatic energy, E'_{pol} is the polarization energy, E'_{dis} is the dispersion energy and E'_{rep} is the repulsive energy. *k*'s in the above equation are the scale factors corresponding to the molecular energies obtained from the generated wave function using density functional theory. Further, the interaction energies were employed to construct '3D-energy frameworks' and to visualize the packing of the molecules in the molecular crystal structures[50].

4.7 Density functional theory (DFT) calculations

DFT calculations have been performed for both initial molecules and GA-BU cocrystal hydrate molecule using Gaussian 16[51] and visualized through Gaussview 6.0.16[52]. The geometry and frequency optimization were carried out in the gas phase at B3LYP/6-311+G(d,p) level of theory without any constraints by using the coordinates extracted from the cif file. The Khon-Sham molecular orbitals, molecular electrostatic potential (MEP) map, and molecular energies were obtained from the optimized geometry. Further, the ground state molecular energy gap and related reactive parameters are calculated using Koopman's approximation[53] and the results of the initial molecules were compared with that of the cocrystal hydrate molecule.

4.8 Molecular docking studies

World health organization has affirmed the Covid-19 as an escalating disease on 12th March 2020[54-56]. Several scientific communities are conducting studies on COVID-19 virus concerning a novel therapeutic agent to treat infected patients in worldwide. In this work, our effort is to test the potential of GA-BU cocrystal as an antiviral agent, through molecular docking (MD) analysis. MD study was carried out using MGL tools 1.5.6[57] with AutoDock Vina[58-59] to detect the preferred binding sites. CIF of GA-BU was used for the ligand preparation and the molecule is prepared, optimized and energy minimized. Further, the three-dimensional structure of the main protease (PDB ID:6LU7 is the first deposited main protease structure of the novel COVID-19 which serves as a potential target for the inhibition of COVID-19) was downloaded from the PDB. The initial preparation of the protein structure was performed by removing water and N3 inhibitor using Biovia Discovery Studio 2019 visualizer[60]. Then using AutoDock Tools nonpolar hydrogen atoms were added and energy was minimized to the main protease. The atomic potential binding site was defined using grid size of x = -11.575, y = 14.611 and z = 65.164. The binding affinity of the GA-BU was observed as a negative score with the unit of kcal/mole. The ligand interactions were visualized and analyzed using Biovia Discovery Studio 2019 visualizer.

References

1. Dhanaraj, G., Byrappa, K., Prasad, V. V., & Dudley, M. (2010). Crystal growth techniques and characterization: an overview. *Springer Handbook of Crystal Growth*, 3-16. https://link.springer.com/chapter/10.1007/978-3-540-74761-1_1
2. Garside, J. (1971). The concept of effectiveness factors in crystal growth. *Chemical Engineering Science*, *26*(9), 1425-1431. https://doi.org/10.1016/0009-2509(71)80062-3
3. Brandeis, G., Jaupart, C., & Allègre, C. J. (1984). Nucleation, crystal growth and the thermal regime of cooling magmas. *Journal of Geophysical Research: Solid Earth*, *89*(B12), 10161-10177. https://doi.org/10.1029/JB089iB12p10161
4. Myerson, A. S., & Ginde, R. (2002). Crystals, crystal growth, and nucleation. In *Handbook of industrial crystallization* (pp. 33-65). Butterworth-Heinemann. https://doi.org/10.1016/B978-075067012-8/50004-5
5. Sankaranarayanan, K., & Ramasamy, P. (2005). Unidirectional seeded single crystal growth from solution of benzophenone. *Journal of Crystal Growth*, *280*(3-4), 467-473. https://doi.org/10.1016/j.jcrysgro.2005.03.075
6. Schultheiss, N., & Newman, A. (2009). Pharmaceutical cocrystals and their physicochemical properties. *Crystal growth and design*, *9*(6), 2950-2967. https://doi.org/10.1021/cg900129f
7. Newman, A. W., & Byrn, S. R. (2003). Solid-state analysis of the active pharmaceutical ingredient in drug products. *Drug discovery today*, *8*(19), 898-905. https://doi.org/10.1016/S1359-6446(03)02832-0
8. Cheney, M. L., Weyna, D. R., Shan, N., Hanna, M., Wojtas, L., & Zaworotko, M. J. (2011). Coformer selection in pharmaceutical cocrystal development: a case study of a meloxicam aspirin cocrystal that exhibits enhanced solubility and pharmacokinetics. *Journal of pharmaceutical sciences*, *100*(6), 2172-2181. https://doi.org/10.1002/jps.22434
9. Kumar, S. (2018). Pharmaceutical cocrystals: an overview. *Indian Journal of Pharmaceutical Sciences*, *79*(6), 858-871.
10. Jyothi, K. L., Kumara, K., Hema, M. K., Gautam, R., Row, T. G., & Lokanath, N. K. (2020). Structural elucidation, theoretical insights and thermal properties of three novel multicomponent molecular forms of gallic acid with hydroxypyridines. *Journal of Molecular Structure*, *1207*, 127828. https://doi.org/10.1016/j.molstruc.2020.127828
11. Ganduri, R., Cherukuvada, S., & Guru Row, T. N. (2015). Multicomponent adducts of pyridoxine: an evaluation of the formation of eutectics and molecular salts. *Crystal Growth & Design*, *15*(7), 3474-3480. https://doi.org/10.1021/acs.cgd.5b00546
12. Newman, A. W., & Byrn, S. R. (2003). Solid-state analysis of the active pharmaceutical ingredient in drug products. *Drug discovery today*, *8*(19), 898-905. https://doi.org/10.1016/S1359-6446(03)02832-0
13. Nayeem, N., Asdaq, S. M. B., Salem, H., & AHEl-Alfqy, S. (2016). Gallic acid: a promising lead molecule for drug development. *Journal of Applied Pharmacy*, *8*(2), 1-4. https://doi.org/10.4172/1920-4159.1000213
14. Chen, H. M., Wu, Y. C., Chia, Y. C., Chang, F. R., Hsu, H. K., Hsieh, Y. C., ... & Yuan, S. S. (2009). Gallic acid, a major component of Toona sinensis leaf extracts, contains a ROS-mediated anti-cancer activity in human prostate cancer cells. *Cancer letters*, *286*(2), 161-171. https://doi.org/10.1016/j.canlet.2009.05.040
15. Borges, A., Saavedra, M. J., & Simões, M. (2012). The activity of ferulic and gallic acids in biofilm prevention and control of pathogenic bacteria. *Biofouling*, *28*(7), 755-767. https://doi.org/10.1080/08927014.2012.706751
16. Seo, D. J., Lee, H. B., Kim, I. S., Kim, K. Y., Park, R. D., & Jung, W. J. (2013). Antifungal activity of gallic acid purified from Terminalia nigrovenulosa bark against Fusarium solani. *Microbial pathogenesis*, *56*, 8-15. https://doi.org/10.1016/j.micpath.2013.01.001
17. Kratz, J. M., Andrighetti-Fröhner, C. R., Leal, P. C., Nunes, R. J., Yunes, R. A., Trybala, E., ... & Simões, C. M. O. (2008). Evaluation of anti-HSV-2 activity of gallic acid and pentyl gallate. *Biological and Pharmaceutical Bulletin*, *31*(5), 903-907. https://doi.org/10.1248/bpb.31.903
18. Kroes, B. V., Van den Berg, A. J. J., Van Ufford, H. Q., Van Dijk, H., & Labadie, R. P. (1992). Anti-inflammatory activity of gallic acid. *Planta medica*, *58*(06), 499-504. https://doi.org/10.1055/s-2006-961535
19. Jyothi, K. L., Gautam, R., Swain, D., Guru Row, T. N., & Lokanath, N. K. (2019). Cocrystals of gallic acid with urea and propionamide: supramolecular structures, Hirshfeld surface analysis, and DFT studies. *Crystal Research and Technology*, *54*(8), 1900016. https://doi.org/10.1002/crat.201900016
20. Chadha, R., Saini, A., Khullar, S., Jain, D. S., Mandal, S. K., & Guru Row, T. N. (2013). Crystal structures and physicochemical properties of four new lamotrigine multicomponent forms. *Crystal growth & design*, *13*(2), 858-870. https://doi.org/10.1021/cg301556j
21. Lama, A., Annunziata, C., Coretti, L., Pirozzi, C., Di Guida, F., Izzo, A. N., ... & Raso, G. M. (2019). N-(1-carbamoyl-2-phenylethyl) butyramide reduces antibiotic-induced intestinal injury, innate immune activation and modulates microbiota composition. *Scientific reports*, *9*(1), 1-12. https://www.nature.com/articles/s41598-019-41295-x
22. Kamal, A., Tamboli, J. R., Ramaiah, M. J., Adil, S. F., Koteswara Rao, G., Viswanath, A., ... & Pal-Bhadra, M. (2012). Anthranilamide–Pyrazolo [1, 5-a] pyrimidine Conjugates as p53 Activators in Cervical Cancer Cells. *ChemMedChem*, 7(8), 1453-1464. https://doi.org/10.1002/cmdc.201200205
23. Wolff, S. K., Grimwood, D. J., McKinnon, J. J., Turner, M. J., Jayatilaka, D., & Spackman, M. A. (2012). CrystalExplorer (Version 3.1). *University of Western Australia*. http://crystalexplorer.scb.uwa.edu.au/
24. Kamat, V., Kumara, K., Naik, K., Kotian, A., Netalkar, P., Shivalingegowda, N., ... & Revankar, V. (2017). [Dichlorido (2-(2-(1H-benzo [d] thiazol-2-yl) hydrazono) propan-1-ol) Cu (II)]: Crystal structure, Hirshfeld surface analysis and

correlation of its ESI-MS behavior with [Dichlorido 3-(hydroxyimino)-2-butanone-2-(1H-benzo [d] thiazol-2-yl) hydrazone Cu (II)]. *Journal of Molecular Structure*, 1149, 357-366. https://doi.org/10.1016/j.molstruc.2017.07.109

25. Seth, S. K. (2013). Tuning the formation of MOFs by pH influence: X-ray structural variations and Hirshfeld surface analyses of 2-amino-5-nitropyridine with cadmium chloride. *Cryst Eng Comm*, 15(9), 1772-1781. https://doi.org/10.1039/C2CE26682B
26. Seth, S. K. (2014) *J. Mol. Stru*. 1064, 70-75.
27. McKinnon, J. J., Jayatilaka, D., & Spackman, M. A. (2007). Towards quantitative analysis of intermolecular interactions with Hirshfeld surfaces. *Chemical Communications,* (37), 3814-3816. https://doi.org/10.1039/B704980C
28. Kamat, V., Kumara, K., Shaikh, S., Shivalingegowda, N., Lokanath, N. K., & Revankar, V. (2018). Crystal structure and Hirshfeld surface analysis of bis (2-(2-(1H-benzo [d] imidazol-2-yl) hydrazono) propan-1-ol) nickel (II) chloride. *Chemical Data Collections*, 17, 251-262. https://doi.org/10.1016/j.cdc.2018.09.004
29. M. W. Shi, S. P. Thomas, G. A. Koutsantonis and M. A. Spackman, *Cryst. Growth Des*, 15 (12) (2015) 5892-5900.
30. Mohamooda Sumaya, U., KarunaKaran, J., Biruntha, K., MohanaKrishnan, A. K., & Usha, G. (2018). Crystal structure and Hirshfeld surface analysis and energy frameworks of 1-(2, 4-dimethylphenyl)-4-(4-methoxyphenyl) naphthalene. Acta Crystallographica Section E: Crystallographic Communications, 74(7), 939-943. https://doi.org/10.1107/S2056989018008332
31. Mackenzie, C. F., Spackman, P. R., Jayatilaka, D., & Spackman, M. A. (2017). CrystalExplorer model energies and energy frameworks: extension to metal coordination compounds, organic salts, solvates and open-shell systems. *IUCrJ,* 4(5), 575-587. https://doi.org/10.1107/S205225251700848X
32. Kumara, K., Al-Ostoot, F. H., Mohammed, Y. H. E., Khanum, S. A., & Lokanath, N. K. (2019). Synthesis, crystal structure and 3D energy frameworks of ethyl 2-[5-nitro-2-oxopyridine-1 (2H)-yl] acetate: Hirshfeld surface analysis and DFT calculations. *Chemical Data Collections*, 20, 100195. https://doi.org/10.1016/j.cdc.2019.100195 .
33. Raveesha, T. C., Hema, M. K., Pampa, K. J., Chandrashekara, P. G., Mantelingu, K., Demappa, T., & Lokanath, N. K. (2021). Analysis of supramolecular self-assembly of two chromene derivatives: Synthesis, crystal structure, Hirshfeld surface, quantum computational and molecular docking studies. *Journal of Molecular Structure*, 1225, 129104. https://doi.org/10.1016/j.molstruc.2020.129104
34. Trask, A. V., & Jones, W. (2005). Crystal engineering of organic cocrystals by the solid-state grinding approach. *Organic solid state reactions*, 41-70. https://doi.org/10.1007/b100995
35. Karki, S., Friščić, T., Jones, W., & Motherwell, W. S. (2007). Screening for pharmaceutical cocrystal hydrates via neat and liquid-assisted grinding. *Molecular pharmaceutics*, *4*(3), 347-354. https://doi.org/10.1007/b100995
36. Hasa, D., Schneider Rauber, G., Voinovich, D., & Jones, W. (2015). Cocrystal Formation through Mechanochemistry: from Neat and Liquid-Assisted Grinding to Polymer-Assisted Grinding. *Angewandte Chemie*, *127*(25), 7479-7483. https://doi.org/10.1002/ange.201501638
37. Schultheiss, N., & Newman, A. (2009). Pharmaceutical cocrystals and their physicochemical properties. *Crystal growth and design*, *9*(6), 2950-2967. https://doi.org/10.1021/cg900129f
38. Weyna, D. R., Shattock, T., Vishweshwar, P., & Zaworotko, M. J. (2009). Synthesis and structural characterization of cocrystals and pharmaceutical cocrystals: mechanochemistry vs slow evaporation from solution. *Crystal Growth and Design*, *9*(2), 1106-1123. https://doi.org/10.1021/cg800936d
39. Newman, A. W., & Byrn, S. R. (2003). Solid-state analysis of the active pharmaceutical ingredient in drug products. *Drug discovery today*, *8*(19), 898-905. https://doi.org/10.1016/S1359-6446(03)02832-0
40. Jyothi, K. L., & Lokanath, N. K. (2020). Understanding the Formation of Novel Hydrated Gallic Acid-Creatinine Molecular Salt: Crystal Structure, Hirshfeld Surface and DFT Studies. *Journal of Chemical Crystallography*, *50*(4), 410-421. https://doi.org/10.1007/s10870-019-00814-4
41. Bruker, S. P. (2009). Bruker AXS Inc., Madison, Wisconsin, USA, 1999;(b) AL Spek. *Acta Crystallogr., Sect. D: Biol. Crystallogr*, 65, 148-155.
42. Sheldrick, G. M. (2015). Crystal structure refinement with SHELXL. *Acta Crystallographica Section C: Structural Chemistry,* 71(1), 3-8. https://doi.org/10.1107/S2053229614024218 Sheldrick, G. M. (1990). Phase annealing in SHELX-90: direct methods for larger structures. *Acta Crystallographica Section A: Foundations of Crystallography,* 46(6), 467-473. https://doi.org/10.1107/S0108767390000277
43. Spek, A. L. (1990) PLATON, an integrated tool for the analysis of the results of a single crystal structure determination, *Acta. Cryst. A*. 46, 34. https://doi.org/10.1107/S0108767390099780
44. Macrae, C. F., Bruno, I. J., Chisholm, J. A., Edgington, P. R., McCabe, P., Pidcock, E., ... & Wood, P. A. (2008). Mercury CSD 2.0–new features for the visualization and investigation of crystal structures. *Journal of Applied Crystallography*, 41(2), 466-470. https://doi.org/10.1107/S0021889807067908
45. Sarkar, A., & Rohani, S. (2015). Cocrystals of acyclovir with promising physicochemical properties. *Journal of pharmaceutical sciences*, *104*(1), 98-105. https://doi.org/10.1002/jps.24248

46. Seth, S. K. (2014). Structural elucidation and contribution of intermolecular interactions in O-hydroxy acyl aromatics: Insights from X-ray and Hirshfeld surface analysis. Journal of *Molecular Structure*, 1064, 70-75. https://doi.org/10.1016/j.molstruc.2014.01.068
47. Spackman, M. A., & McKinnon, J. J. (2002). Fingerprinting intermolecular interactions in molecular crystals. *CrystEngComm*, 4(66), 378-392. https://Doi.org/10.1039/B203191B
48. McKinnon, J. J., Jayatilaka, D., & Spackman, M. A. (2007). Towards quantitative analysis of intermolecular interactions with Hirshfeld surfaces. *Chemical Communications*, (37), 3814-3816. https://doi.org/10.1039/B704980C
49. Kumara, K., Shivalingegowda, N., Mahadevaswamy, L. D., Kariyappa, A. K., & Lokanath, N. K. (2017). Crystal structure studies and Hirshfeld surface analysis of 5-(4-methoxyphenyl)-3-(thiophen-2-yl)-4, 5-dihydro-1H-pyrazole-1-carbothioamide. Chemical *Data Collections*, 9, 251-262. https://doi.org/10.1016/j.cdc.2016.11.006
50. Kumara, K., Jyothi, M., Shivalingegowda, N., Khanum, S. A., & Krishnappagowda, L. N. (2017). Synthesis, characterization, crystal structure and Hirshfeld surface analysis of 1-(4-ethoxyphenyl)-3-(4-methylphenyl) prop-2en-1-one. *Chemical Data Collections*, 9, 152-163. https://doi.org/10.1016/j.cdc.2017.06.003
51. Frisch, M. J., Trucks, G. W., Schlegel, H. B., Scuseria, G. E., Robb, M. A., Cheeseman, J. R., ... & Fox, D. J. (2016). Gaussian 16.
52. R. Dennington, T. Keith, J.Millam, GaussView, version 6. Semichem Inc.: Shawnee Mission, KS. (2009).
53. Koopmans, T. (1934). Über die Zuordnung von Wellenfunktionen und Eigenwerten zu den einzelnen Elektronen eines Atoms. *physica*, 1(1-6), 104-113.
54. Havranek, B., & Islam, S. M. (2021). An in silico approach for identification of novel inhibitors as potential therapeutics targeting COVID-19 main protease. *Journal of Biomolecular Structure and Dynamics*, 39(12), 4304-4315. https://doi.org/10.1080/07391102.2020.1776158
55. Bheenaveni, R. S. (2020). India's indigenous idea of herd immunity: the solution for COVID-19?. *Traditional Medicine Research*, 5(4), 182. https://doi.org/10.12032/TMR20200519181
56. Dong, E., Du, H., & Gardner, L. (2020). An interactive web-based dashboard to track COVID-19 in real time. *The Lancet infectious diseases*, 20(5), 533-534. https://doi.org/10.1016/S1473-3099(20)30120-1
57. Agrahari, A. K. (2017). A computational approach to identify a potential alternative drug with its positive impact toward PMP22. *Journal of Cellular Biochemistry*, *118*(11), 3730-3743.
58. Trott, O., and Olson, A. J. (2010). AutoDock Vina: improving the speed and accuracy of docking with a new scoring function, efficient optimization, and multithreading. *Journal of computational chemistry*, 31(2), 455-461. https://doi.org/10.1002/jcb.26020
59. Huey, R., Morris, G. M., & Forli, S. (2012). Using AutoDock 4 and AutoDock vina with AutoDockTools: a tutorial. *The Scripps Research Institute Molecular Graphics Laboratory*, 10550, 92037.
60. Hema, M. K., ArunRenganathan, R. R., Nanjundaswamy, S., Karthik, C. S., Mohammed, Y. H. I., Alghamdi, S., ... & Mallu, P. (2020). N-(4-bromobenzylidene)-2, 3-dihydrobenzo [b][1, 4] dioxin-6-amine: Synthesis, crystal structure, docking and in-vitro inhibition of PLA2. *Journal of Molecular Structure*, 1218, 128441. https://doi.org/10.1016/j.molstruc.2020.128441